Fresnel rhombs as achromatic phase shifters for infrared nulling interferometry

Dimitri Mawet[1], Charles Hanot[1], Cédric Lenaerts[1], Pierre Riaud[3], Denis Defrère[1], Denis Vandormael[2], Jérôme Loicq[2], Karl Fleury[2], Jean-Yves Plesseria[2], Jean Surdej[1] and Serge Habraken[1,2]

[1]*University of Liège, 17 allée du 6 Août, B-4000, Sart Tilman, Belgium*
[2]*Centre Spatial de Liège, Avenue du Pré-Aily, B-4031, Liège-Angleur, Belgium*
[3]*Observatoire de Paris-Meudon, 5 place Jules Janssen, 92190 Meudon, France*

mawet@astro.ulg.ac.be

Abstract: We propose a new family of achromatic phase shifters for infrared nulling interferometry. These key optical components can be seen as optimized Fresnel rhombs, using the total internal reflection phenomenon, modulated or not. The total internal reflection indeed comes with a phase shift between the polarization components of the incident light. We propose a solution to implement this vectorial phase shift between interferometer arms to provide the destructive interference process needed to disentangle highly contrasted objects from one another. We also show that, modulating the index transition at the total internal reflection interface allows compensating for the intrinsic material dispersion in order to make the subsequent phase shift achromatic over especially broad bands. The modulation can be induced by a thin film of a well-chosen material or a subwavelength grating whose structural parameters are thoroughly optimized. We present results from theoretical simulations together with preliminary fabrication outcomes and measurements for a prototype in Zinc Selenide.

OCIS codes: (120.3180) Interferometry; (050.5080) Phase Shift.

References and links

1. R.N. Bracewell, "Detecting Non Solar Planets by Spinning Infrared Interferometer," Nature **274,** 780–781 (1978).
2. A. Léger, J.M. Mariotti, B. Mennesson, M. Ollivier, J.L. Puget, D. Rouan, J. Schneider, "Could We Search for Primitive Life on Extrasolar Planets in the Near Future," Icarus **123,** 249–255 (1996).
3. A.L. Mieremet, J.J. Braat, H. Bokhove, K. Ravel, "Achromatic phase shifting using adjustable dispersive elements," Proc. SPIE **4006**, 1035–1041 (2000).
4. J. Gay, Y. Rabbia, "Principe d'un coronographe interférentiel," C. R. Acad. Sci. Paris **322**, 265–271 (1996).
5. E. Serabyn, M.M. Colavita, "Fully Symmetric Nulling Beam Combiners," Appl. Opt. **40**, 1668–1671 (2001).
6. B. Chazelas, F. Brachet, P. Bordé, B. Mennesson, M. Ollivier, O. Absil, A. Labèque, C. Valette, A. LégerA., "Instrumental stability requirements for exoplanet detection with a nulling interferometer: variability noise as a central issue," Appl. Opt. **45**, 984–992 (2006).
7. F. Hénault, "Design of achromatic phase shifters for spaceborne nulling interferometry," Opt. Lett. **31**, 3635–3637 (2006).
8. C. Hanot et al., Proc. SPIE **6693-62**, in press (2007).
9. A.L. Karlsson, O. Wallner, J.M. Perdigues Armengol, O. Absil,"Three telescope nuller based on multibeam injection into single-mode waveguide," Proc. SPIE **5491**, 831–841 (2004).
10. D. Mawet, C. Lenaerts, P. Riaud, J. Surdej, S. Habraken, D. Vandormael, "Use of subwavelength gratings in TIR incidence as achromatic phase shifters," Opt. Express **13,** 8686–8691 (2005).

11. M.G. Moharam and T.K Gaylord, "Rigourous Coupled-Wave Analysis of planar grating diffraction," J. Opt. Soc. Am. **71**, 811–818 (1981).
12. M. Born & E. Wolf, "Reflection and refraction of a plane wave," in *Principles of Optics* eds. (Cambridge University press, seventh edition, 1997), 49–53.
13. K. B. Rochford, A. H. Rose, P. A. Williams, C. M. Wang, I. G. Clarke, P. D. Hale, G. W. Day, "Design and performance of a stable linear retarder," Appl. Opt. **36**, 6458–6465 (1997).
14. R. Anderson, "Quarterwaveplate and Fresnel rhomb compared in the 10-Mum CO2 laser emission region," Appl. Opt. **27**, 2746–2747 (1988).
15. P. Clapham, M. Downs, R. King, "Some applications of thin films to polarization devices," Appl. Opt. **8**, 1965–1974 (1969).
16. J.C. Lagarias, J. A. Reeds, M. H. Wright, and P. E. Wright, "Convergence Properties of the Nelder-Mead Simplex Method in Low Dimensions," SIAM Journal of Optimization **9** (1), 112–147 (1998).
17. Gary J. Hawkins, *Spectral Characterisation of Infrared Optical Materials and Filters* (PhD Thesis - The University of Reading UK, 1998).
18. F. Peter, Z Phys **15**, 358-368 (1923).
19. W. J. Tropf, "Temperature-dependent refractive index models for BaF2, CaF2, MgF2, SrF2, LiF, NaF, KCl, ZnS and ZnSe," Opt. Eng. **34**, 1369–1373 (1995).
20. W. J. Tropf, M.E. Thomas, M.J. Linevsky, "Infrared refractive indices and thermo-optic coefficients for several materials," Proc. SPIE **3425**, 160–171 (1998).
21. A. Labèque, B. Chazelas, F. Brachet, C. Commeaux, P. Blache, A. Léger, M. Ollivier, T. Lepine, C. Valette, "The Nulltimate project: building and testing, at low temperature, achromatic phase shifters to prepare the Darwin mission," Proc. SPIE **5491**, 999–1010 (2004).
22. P. Lalanne, P. Pichon, P. Chavel, E. Cambril, H. Launois, "Interferometric Characterization of Subwavelength Lamellar Gratings," Appl. Opt. **38,** 4980–4984 (1999).
23. W. R. Chen, S. J. Chang, Y. K. Su et al., "Refractive Ion Etching of ZnSe, ZnSSe, ZnCdSe and ZnMgSSe by H2/Ar and CH4/H2/AR," Jpn. J. Appl. Phys. **39,** 3308–3313 (2000).
24. K. Kurisu, T. Hirai, K. Fuse et al., "Development of a Diffractive Optical Element for Laser Processing," SEI Technical Review **53,** 86–91 (2002).
25. G.R. Mariner and K. Vedam, "Stress-optic coefficient of ZnSe at 10.6 microns," Appl. Opt. **20**, 2878–2879 (1981).
26. C. Yang and P. Yeh, "Artificial uniaxial and biaxial dielectrics with the use of photoinduced gratings," J. Appl. Phys. **81,** 23–29 (1997).

1. Introduction

Despite the tremendous progress in the indirect detection techniques and the increasing number of detected extrasolar planetary objects, exoplanet hunters are still struggling with the technical challenges hampering the conception of an observatory that will allow the direct imaging and characterization of Earth-like planets. Indeed, even best telescopes can't see them directly because of the large flux ratio between the planet and its parent star. For example, an Earth-like exoplanet is typically $\sim 10^9$ times fainter than its host star in the visible spectrum, $\sim 10^6$ in the thermal infrared. Among all raised ideas to reach the needed very high dynamic range, such as visible coronagraphy, infrared nulling interferometry proposed by R. Bracewell in 1978 [1] appears to be a most promising technique. The nulling interferometry consists in adjusting the phases (with a π phase shift in the two-telescope case) of the beams coming from various telescopes (two or more) to produce a fully destructive interference on the optical axis, nulling the starlight while letting the planetary signal pass through.

One of the most critical units of a nulling interferometer is the phase shifter. The difficulty is to conceive it to perform well enough over the whole operational spectral range. Remotely characterizing exoplanet atmospheres, which is our ultimate goal, requires spectroscopic analysis over large spectral bands. For example, the Darwin Infrared Space Interferometer [2] considered by the European Space Agency (ESA), or the Terrestrial Planet Finder-Interferometer (TPF-I) considered by NASA, will operate in the infrared wavelength range spanning from 6 to 18 (or 20) micrometers. Several studies have been initiated by both agencies, with the purpose of selecting the best achromatic phase shifter (APS). Exhaustive listing or detailed trade-off between different existing APS is beyond the scope of this paper. However, let us cite the four

most promising concepts that are currently being examined:

- the dispersive plate APS [3], directly inspired by the techniques used by optical designers to minimize lens chromatic aberrations, uses a given number of glass or dielectric plates, whose materials and thicknesses are optimized together with the free-air optical path difference (OPD), mutually neutralizing the various dispersion gradients to produce a given phase shift over the desired spectral band;

- the focus-crossing APS [4], where an achromatic phase shift of π is produced by making the beam cross a focus along one of the interferometer arm;

- the field-reversal APS [5], which is based on the achromatic reversal of the electric-field vector on one of the two interfering waves, by means of a rotational shearing interferometer with a fixed shear of 180 degrees;

- the vectorial APS, subject of this paper, which consists in spatially distributing a phase retardance that is primarily affecting the orthogonal polarization components.

According to [6], for an interferometer with stellar leakages similar to those of a Bracewell two-telescope interferometer, a sensible value for the mean instrumental leakage contribution to the null depth would be

$$N(\lambda) = 10^{-5} \left(\frac{\lambda}{7\,\mu m} \right)^{3.37} \tag{1}$$

In addition to the APS imperfections there are many systematic sources of deterioration of the null depth: e.g., telescope pointing errors, photometric unbalance, OPD errors, etc. Consequently, the requirement for the limitation on the null depth due to the APS alone, must be significantly lower than expressed in Eq. 1, i.e., $N = 10^{-6}$ or better. In practice, we will always apply a reasonable security coefficient for the performances of the APS by requiring a few 10^{-7}.

As we will show, the vectorial APS family is a promising alternative to the three first mentioned APS. Indeed, as compared to the difficulty of finding the dispersive plate APS working point, the vectorial APS implementation is straightforward. Moreover, unlike the focus-crossing and field-reversal APS, vectorial APS do not come with a subsequent pupil flip. The pupil inversion, creating a pair of images for one single planet, induces several limitative consequences. First, the spatial coherence γ of the interfering beams must be of the order of the null specification on the APS, i.e. $\gamma \leq 10^{-6}$. Second, Hénault [7] recently stressed out that the pupil-flip APS could be less favorable because the pupil inversion seems to substantially impact extinction maps, implying S/N losses and weakening the detection capacity of the instrument [8]. These problems can only be mitigated with monomode spatial filtering. Third, contrary to the mirror APS which only provides a π phase shift (some interferometer configurations require other phase shift values), the vectorial APS is theoretically able to satisfy any requirements in this respect. For instance, it could provide the 90°, 120° and 240° phase shifts required by the three telescope nuller [9] (TTN), either in the planar or non-planar configuration.

We recently proposed the idea of using subwavelength gratings in total internal reflection (TIR) incidence as achromatic phase shifters [10]. Theoretical calculations using the Rigorous Coupled Wave Analysis [11] (RCWA) pointed to interesting results. The purpose of the present paper is fourfold:

- put the subwavelength grating in TIR incidence APS in the more general context of modulated Fresnel rhomb APS for infrared nulling interferometry;

- presenting a general tolerance study of Fresnel rhomb-based vectorial APS;

- introducing some manufacturing and design considerations for the actual prototype under fabrication at CSL ("Centre Spatial de Liège") to be tested at room (298 K) and cryogenic (100 K) temperatures at IAS ("Institut d'Astrophysique Spatiale", Orsay, France);

- presenting some preliminary retardance measurement results obtained at 632.8 nm.

2. Principles

The TIR phenomenon comes with a phase shift between the vectorial s and p polarization components. This vectorial phase shift takes the following general form [12]

$$\Delta\phi_{s-p} = 2\arctan\left[\frac{\sqrt{\sin^2\theta - n_{ti}^2}}{n_{ti}^2\cos\theta}\right] - 2\arctan\left[\frac{\sqrt{\sin^2\theta - n_{ti}^2}}{\cos\theta}\right] \tag{2}$$

where θ is the angle of incidence, greater or equal to θ_c, the critical angle defined as $\sin\theta_c = n_{ti} = n_t/n_i$ and where n_i and n_t are the refractive indices of the incident and emergent media, respectively. This property is exploited in the well-known Fresnel rhombs, which are retarders to be used alone as polarization optics.

2.1. *Double rhomb configuration*

Single Fresnel rhombs are known to be very sensitive to incidence angle variations (at the sub-arcmin level). This drawback would be penalizing in our application since the thermal infrared interferometric beam is likely to slightly diverge because of diffraction while somewhat wandering around because of vibrations. For this reason, we chose the double rhomb configuration for its known insensitivity to incidence variations [13]. Indeed, the pairs of reflections in the two rhombs are complementary (see Fig. 1 and Fig. 2); an increase in the first two TIR angles due to departure from nominal incidence leads to a decrease in the last two angles. Thus if the phase shift varies linearly with the TIR angle, the retardance changes are cancelled. Therefore a wider range of incidence angle variations can be tolerated: up to several degrees.

2.2. *Modulated total internal reflection achromatic phase shifter*

Classical Fresnel rhombs are limited by the intrinsic index dispersion of the rhomb bulk material [14]. Engraving a subwavelength grating on the TIR interface or simply depositing a single thin layer of a well chosen material leads to a significant improvement. Indeed, the electromagnetic field evanescent interaction with the optimized micro-structure or thin film allows us to tune the index ratio of Eq. 2. It is to be noted that in the double rhomb configuration, the number of subwavelength gratings to be imprinted (resp. thin film to be deposited) on the TIR interface

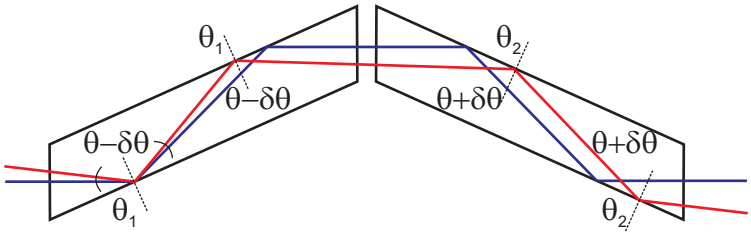

Fig. 1. This scheme shows the double-rhomb configuration. θ_1 (resp. θ_2) is the angle of incidence upon the TIR interfaces of the first (resp. second) rhomb.

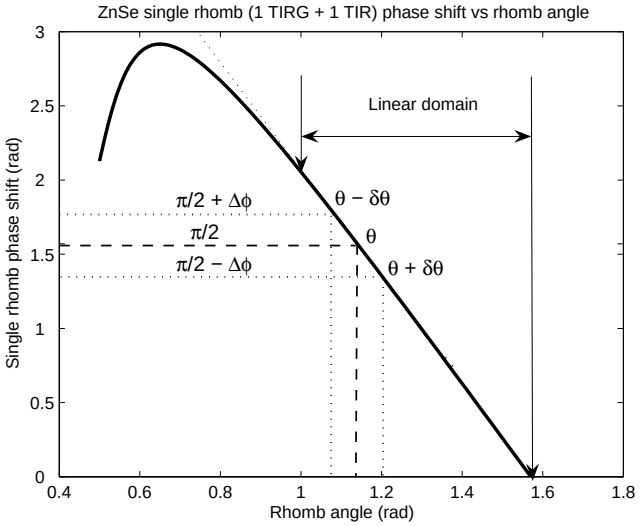

Fig. 2. The double-rhomb geometry allows incidence-angle variations $\delta\theta$ to be compensated by the angle complementarity between the two rhombs and the linearity of the phase shift with respect to the rhomb angle. The linearity is present in the bare Fresnel rhomb or the TIR modulated one.

may be limited to only two out of four. Indeed, the dispersion compensation artificially introduced by the modulated interface can already and substantially improve the global behavior of the component in terms of phase shift achromaticity.

2.2.1. Total internal reflection grating

The principle of the total internal reflection grating achromatic phase shifter (TIRG APS) is to use a subwavelength grating in the TIR incidence condition [10]. One dimensional subwavelength gratings turn out to be artificially anisotropic [10]. It means that the structure can be associated with two synthetic effective indices, one for each polarization component: TE (transverse electric, vibrating parallel to the grating grooves, or s) and TM (transverse magnetic, vibrating perpendicular to the grooves, or p). These effective indices, n_{TE} and n_{TM} are totally dependent on the grating and incidence geometries (see Fig. 5), which can be wisely engineered to compensate for the natural material dispersion.

2.2.2. Total internal reflection thin film

Instead of engraving a subwavelength grating onto the TIR interface, one can deposit a layer of a well-chosen foreign material. The principle of the so-called total internal reflection thin film achromatic phase shifter (TIRTF APS) is to make use of such a thin film coated with an appropriate thickness on the TIR interface. This principle has been known for quite a long time in the visible where MgF_2 thin films are commonly deposited on $BK7$ or Silica rhombs to improve the angular and chromatic behavior of commercial Fresnel rhombs [15].

2.3. Implementation

Implementing two strictly identical π retarders into the two interferometer arms and rotating them by ninety degrees with respect to each other around the interferometer optical axis, is

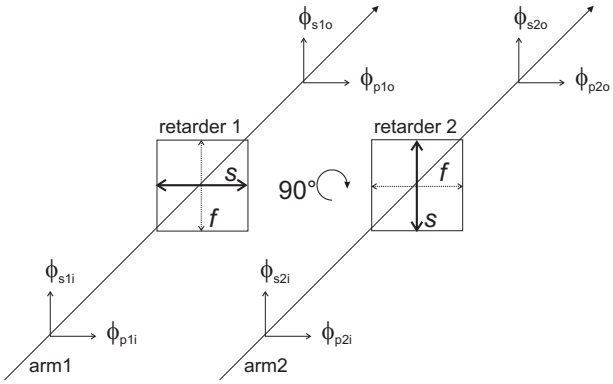

Fig. 3. Implementation of a vectorial phase shifter (retarder) in a two-telescope nulling interferometer (Bracewell). The π retardance between the orthogonal polarizations s and p induced by the light differential optical delay between the slow (s) and fast axis (f) of the vectorial phase shifters 1 and 2 ($\phi_{s1o} - \phi_{p1o} = \phi_{s2o} - \phi_{p2o} = \pi$) can be spatially distributed between the interferometer arms. Indeed, a rotation of 90° of the retarders around the optical axis permutes the role of the polarizations so that at the output, the potentially interfering polarization states, i.e. the parallel ones are in phase opposition, $\phi_{s1o} - \phi_{s2o} = \phi_{p1o} - \phi_{p2o} = \pm\pi$.

a practical solution to spatially distribute the initial vectorial phase shift (see Fig. 3); "vectorial" meaning between the polarization components. The ninety degree rotation between the retarders around the optical axis must be respected at ± 2 arcmin to reach the 10^{-7} secure null depth level.

3. Theoretical analysis

This section is devoted to the theoretical analysis of the TIRG and TIRTF APS. The purpose of this analysis was to optimize (with the "simplex-search" optimization method [16], highly robust when the parameter space is highly discontinuous) the APS component in order to "achromatize" the Darwin/TPF-I working wavelength range: 6-18 μm. However, due to practical constraints like wavefront filtering or dichroic limitations, the latter is expected to be divided into two or three sub-bands. In the two-band case, the first one ranges from 6 to 11 microns while the second one ranges from 11 to 18 microns. Before going into the details of the theoretical analysis, one had to choose the materials according to the bandwidth specifications mentioned here above. Regarding this matter, we immediately had to discard common infrared materials like silicon (*Si*) and gallium arsenide (*GaAs*) for their strong multi-phonon absorption features beginning between 8 and 12 microns [17]. For the same reason, we also had to discard zinc sulphide (*ZnS*) and Germanium (*Ge*), other widespread infrared materials.

The choice for the bulk material constituting the rhomb in fact revealed to be very difficult and severely limited since the material has to be perfectly transparent up to 18 microns (20 if possible) and of course available in large ingots of very good optical quality (good homogeneity, low impurity, etc.). For this reason, we focussed on common infrared material such as zinc selenide (*ZnSe*), cadmium telluride (*CdTe*), and KRS-5. Although *ZnSe* is in general used in the 11-18 μm range, *CdTe* and KRS-5 are the only ones perfectly clear up to 18 microns. Note that *ZnSe*, *ZnS* or even CVD (Chemical Vapor Deposition) Diamond can be used as the layer materials in their phonon absorption ranges since their working thicknesses are very thin and the subsequent absorptions therefore negligible. These selected materials are common in infrared

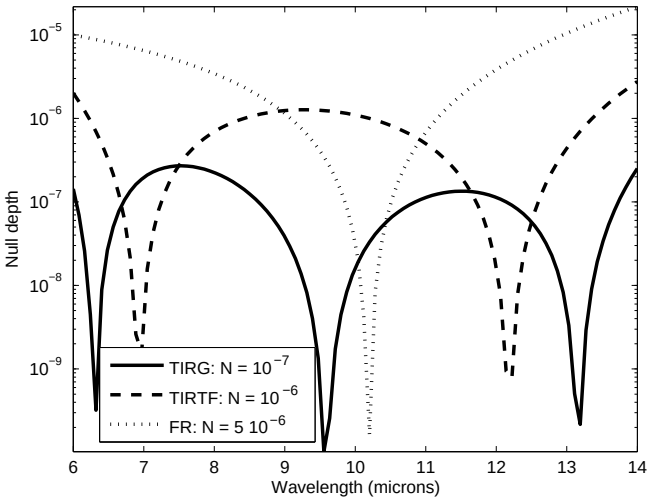

Fig. 4. *ZnSe* double rhomb APS: comparison between Fresnel Rhomb (FR) with non-treated TIR interfaces, TIR thin film (TIRTF) and TIR grating (TIRG). More than substantially improving the global (mean) null depth over the considered wavelength range, the TIRTF and the TIRG solutions significantly decrease the strong leakage at its edges, inevitable with the FR solution.

applications, they cover a large refractive index spectrum ($n = 2-4$) and their processing (polishing, etching, sputtering, etc.) is in general well known for most of them. The refractive index dispersions will be taken from [18] for Diamond, from [19] for *ZnSe*, from [20] for KRS-5 and from [17] for *ZnS*, *CdTe*.

To simulate grating responses in the subwavelength domain, we used an algorithm based on the RCWA, which is also called the Fourier modal method because it is based on Fourier decompositions of the physical characteristics of the grating and fields so that the resolution takes place in the frequency space.

3.1. ZnSe Rhomb

In its polycrystalline form, *ZnSe* is available in large quantities and volumes at a reasonable cost. It is also relatively convenient to polish with very good surface qualities. Moreover, its thermal properties are very attractive, with a low thermal expansion coefficient (7.1×10^{-6}/K) and a rather good thermal conductivity (0.18 W/cm/K). Unfortunately, the chosen double-rhomb configuration inevitably lengthens the optical path in the material. For instance, in the present case, a working angle of about 65.03° would lead to a physical path of about 17 cm inside the material for an entrance beam diameter of 15 mm. In the second Darwin sub-band ($11-18$ μm), such a long path is penalizing since *ZnSe* begins its phonon absorption around 14 microns. Indeed, the absorption coefficient [17] k is equal to 4.24×10^{-6} at 14 μm and 298 K, leading to absorption of about 50%. This value reduces to 2.52×10^{-6} at 100 K, giving an absorption of 30%, which remains acceptable for demonstration purposes. For this reason, a *ZnSe* TIRG APS in the double-rhomb configuration will be practically limited to the $6-14\,\mu$m wavelength range. One of the main outcomes of Table 1 is that the *ZnSe* bare Fresnel rhomb (without any modulation of the TIR interfaces) is not performing well enough for the Darwin

Table 1. Average null depths for the optimized Fresnel double rhomb, TIRG APS, TIRTF APS configurations for the selected infrared materials. D stands for Diamond (CVD).

Rhomb material / band	**Fresnel rhomb**	***TIRG APS***	***TIRTF APS***
ZnSe / $6-11\ \mu$m	2×10^{-6}	1×10^{-8}	D/*ZnS* layer: 1×10^{-7}
ZnSe / $6-14\ \mu$m	6×10^{-6}	1×10^{-7}	D/*ZnS* layer: 1×10^{-6}
CdTe / $6-11\ \mu$m	2×10^{-7}	5×10^{-9}	D/*ZnSe*/*ZnS* layer: 1×10^{-8}
CdTe / $11-18\ \mu$m	8×10^{-7}	1×10^{-8}	D/*ZnSe*/*ZnS* layer: 5×10^{-8}
CdTe / $6-18\ \mu$m	2×10^{-6}	1×10^{-7}	D/*ZnSe*/*ZnS* layer: 5×10^{-7}
KRS-5 / $6-11\ \mu$m	2×10^{-7}	NA	NA
KRS-5 / $11-18\ \mu$m	1×10^{-6}	NA	NA
KRS-5 / $6-18\ \mu$m	2×10^{-6}	NA	NA

baseline 10^{-6} specification (see Fig. 4, dotted line). However, depositing a foreign material at the TIR interface or imprinting a subwavelength grating onto it allows overcoming this limitation in the $6-11\,\mu$m wavelength range. In the larger $6-14\,\mu$m range, only the subwavelength grating solution is able to meet the specification (Fig. 4, continuous line) while the thin film one just misses them by a small factor (Fig. 4, dashed line).

3.2. CdTe Rhomb

Availability of *CdTe* ingots is more limited than *ZnSe* ones. Polishing of *CdTe* is quite delicate but currently under evaluation for improvement by several manufacturers. *CdTe*, which also possesses rather good thermal characteristics (expansion coefficient of 5.9×10^{-6}/K and conductivity of 0.062 W/cm/K), nevertheless appears to be a viable potential solution. Indeed, as already stated, *CdTe* is one of the selected rhomb materials perfectly clear up to 18 microns. Moreover, theoretical RCWA results are excellent, showing better performance than with *ZnSe* (see Table 1). First of all, the *CdTe* bare Fresnel-rhomb solution is worth considering since it is theoretically performing well enough, at least for the Darwin first sub-band but unfortunately not for the second one. Depositing a thin film of a foreign material (e.g., Diamond, *ZnSe* or *ZnS*) overcomes this limitation. As far as the subwavelength grating solution is concerned, results are comfortably in the specifications for both bands. Let us emphasize that there exists a most interesting theoretical solution which would "achromatize" the full Darwin wavelength range from 6 to 18 microns with a single APS consisting of an optimized double *CdTe* rhomb modulated with a subwavelength grating (Table 1).

3.3. KRS-5 Rhomb

KRS-5 infrared dispersion is extremely low [20], making it an ideal material for a Fresnel rhomb. Indeed, results displayed in Table 1 confirm its very good potential. Unfortunately, KRS-5 is a very difficult material to handle. It is toxic, brittle and is not easily polished (to our knowledge its polishing was never demonstrated at qualities better than $\lambda/4$ rms, $\lambda = 632.8$ nm). It is to be emphasized that KRS-5 is common in infrared applications despite its bad thermal conductivity (5.4×10^{-3} W/cm/K) and expansion coefficient (5.8×10^{-5}/K). KRS-5 was also considered since it is one of the rare materials perfectly transparent above 15 microns. Finally, KRS-5 cannot be micro-structured nor easily treated with foreign materials because of its chemical reactivity.

4. Design and tolerancing of a modulated Fresnel rhomb prototype

In this section, we will discuss the design of a modulated Fresnel rhomb prototype intended at being one of the APS selected for study, fabrication and test in the framework of one of ESA's Darwin R&D preparatory activities: Nulltimate [21], which is a project of infrared cryogenic (100 K) nulling testbed. This section will be devoted to the tolerancing of the subwavelength grating and the macroscopic rhomb. The choice of the material for the prototype has been made thanks to a trade-off matrix. Even if *CdTe* shows the best theoretical characteristics in terms of transparency and performances, *ZnSe* was the retained material to make the prototype in the $6-14\,\mu$m Nulltimate wavelength range for the following reasons:

- in its polycrystalline state, *ZnSe* is a priori easy to source, and a convenient material to handle and polish (surface qualities of $\lambda/30$ rms with $\lambda = 632.8$ nm are routinely obtained);
- it is compatible with the thickness-adjustable beam splitters of the Nulltimate test bench which are planned to be in *ZnSe*;
- it is transparent in the optical, letting the *HeNe* 632.8-nm interferometric metrology beam pass through.

4.1. TIRG tolerancing

The fabrication of the TIRG APS will be based on micro-electronic technologies. The first classical step consists in imprinting a photomask of the grating in a photoresist coated on the chosen substrate material. The precision of this step is critical because it defines once and for all the lateral dimensions of the grating (Fig. 5): its period Λ and the so-called feature line, i.e., the period multiplied by the filling factor f. This pattern will then uniformly be transferred into the substrate by an appropriate reactive plasma-beam etching down to the desired depth (h). The fabrication has to be interactive to properly compensate for process errors. In situ monitoring is a possible solution [22] but not the only one as we will discuss.

4.1.1. Manufacturing scenario

Let us now consider the *ZnSe* TIRG APS designed for the 6-14 μm wavelength range. A rough optimization for this range leads to a 900-nm period. Then, assuming this fixed period, best

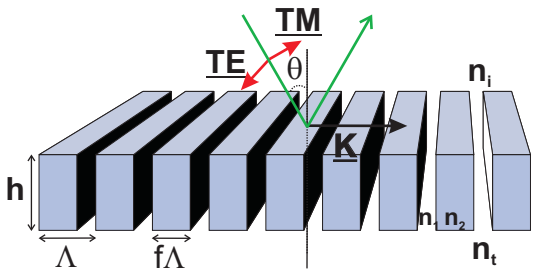

Fig. 5. Schematic of a subwavelength grating. The structure parameters are: the grating vector $|\underline{K}| = 2\pi/\Lambda$, perpendicular to the grating lines, with Λ the spatial period, the thickness h and the filling factor f, such that $f\Lambda$ is the feature line. $\underline{TE}$ and $\underline{TM}$ are the orthogonal polarization components of the θ-incident light. n_i and n_t are the refractive indices of the incident and emergent (transmitting) media, respectively. n_1 and n_2 are the refractive indices of the grating itself (in this case, $n_2 = n_i$ and $n_1 = n_t$).

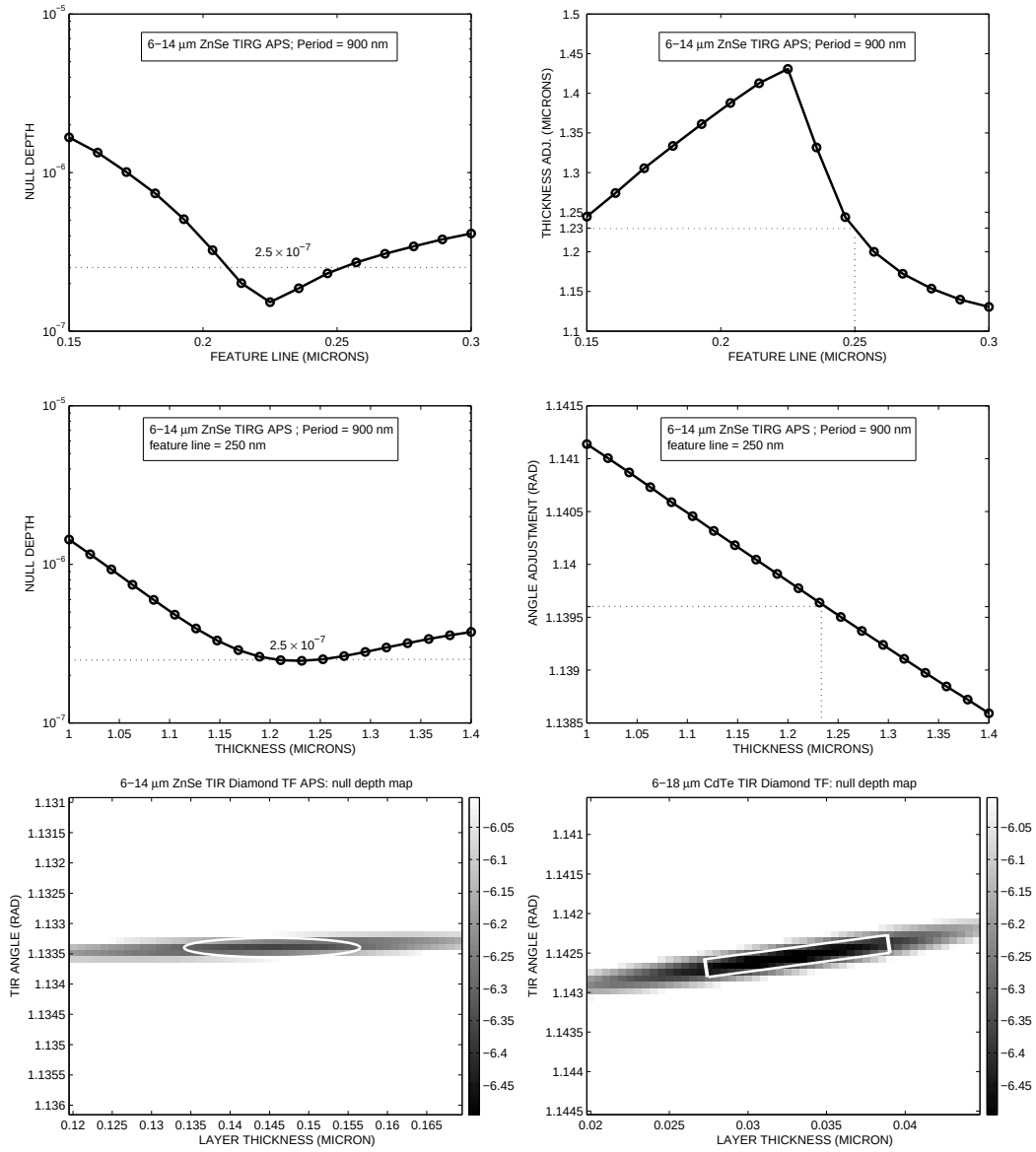

Fig. 6. 6-14 μm *ZnSe* double rhomb APS with 900 nm period. Top left: optimized null depth vs feature line. Top right: thickness adjustment (optimized) vs feature line. Middle left: angle optimized null depth vs thickness for a fixed feature line of 250 nm. Middle right: corresponding angle adjustment (optimized) vs thickness. Bottom: two-dimensional maps of the null depth (log scale, $10^{-\alpha}$) according to the variables "thickness of the layer" and "incidence angle". Left: *ZnSe* TIRTF APS coated with Diamond for the 6 to 14 micron band. Right: *CdTe* TIRTF APS coated with Diamond for the 6 to 18 micron band.

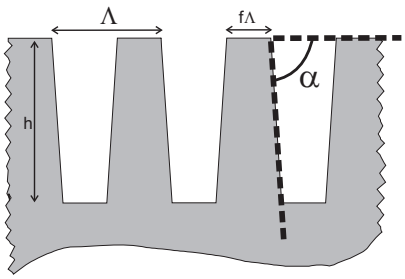

Fig. 7. Trapezoidal profile likely to emerge from the plasma-etching process. The new parameter to be taken into account is the grating slope angle α.

solutions are searched using the "simplex" optimization method [16] coupled to the RCWA algorithm with the filling factor f, the grating thickness h and the incidence angle θ left as free parameters. Results of this optimization are displayed in Fig. 6 (top left), where the optimal null depth is plotted versus the feature line, i.e., the product of the 900-nm fixed period and the varying filling factor. Continuous variations are now imposed to the feature line while letting the optimization algorithm find the corresponding adjustment of the thickness that minimizes the null depth (see 6, top right). The best null depth, in this case the minimum one, is about 1.5×10^{-7}. This optimal value is obtained for the 220-nm feature line. The corresponding adjusted thickness is 1.43 μm. If we calculate the grating aspect ratio, we find 6.5 which is demanding given the nature of the material to be subsequently etched. To relax this difficulty, we chose the conservative width of 250 nm for the feature line which corresponds to an adjusted thickness of 1.23 μm and a subsequently reduced aspect ratio of about 5. Let us now fix the feature line to 250 nm, keep the period at 900 nm and vary the thickness artificially, letting the optimization algorithm find the corresponding incidence polar angle θ adjustment that minimizes the null depth. Results of this analysis are shown in Fig. 6, middle left and right. Provided that the polar angle can be adjusted with a sub-arcmin precision, the $N \approx 2.5 \times 10^{-7}$ tolerance on the thickness definition is 1.23 ± 25 nm, i.e., about 2%, which is feasible.

The conclusion of this tolerance analysis is that, provided that there are interactions between measurements and manufacturing at each key step, the tolerances on the parameter definitions are rather comfortable, up to a few tens of nanometers for the feature line and the thickness. A posteriori correction is reported on the incidence angle which is very convenient since the double rhomb geometry still ensures the insensitivity to the entrance beam incidence configuration (input angle and beam divergence, for instance) at the macroscopic level.

4.1.2. Grating slope angle

Departure from the nominal assumed grating profile, i.e. a perfectly rectangular one, is likely to naturally emerge from the plasma-beam etching process (Fig. 7). The calculated tolerance on the grating slope angle α is 5°, which is very tight and necessitates very directional and anisotropic plasma etching processes.

4.2. TIRTF tolerancing

As far as an eventual TIRTF APS component is concerned, tolerancing can be envisaged in another way. Since the parameter space is limited to two variables, i.e. the thickness of the layer and the angle of incidence, the working points can be traced in two-dimensional maps. From Fig. 6 bottom, we can conclude that the tolerance on the thickness is of $\sim 10\%$. It is to be

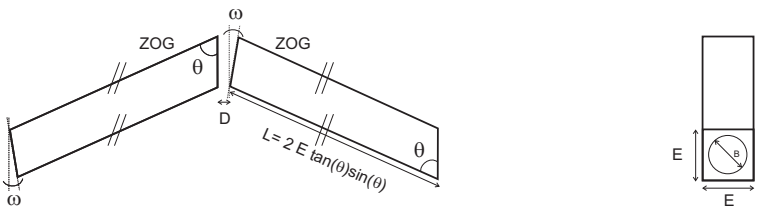

Fig. 8. Double-rhomb geometrical scheme and definition of the wedge angle w.

noted that coatings are routinely deposited with a precision of $\sim 1\%$ on the thicknesses.

4.3. Surface roughness and material homogeneity

We have conducted a complete tolerancing study of roughness and homogeneity effects using a Monte-Carlo method coupled with rigorous diffraction analysis. The conclusion is that the surface roughness and grating thickness variability should not exceed 10 nm rms. Concerning linewidth roughness (feature line uniformity), it should not depart from 25 nm rms. As far as material refractive index homogeneity (δn) is concerned, the conclusion is that the current *ZnSe* synthesizing method (CVD) provides an excellent optical quality ($\delta n \approx 3 \times 10^{-6}$) that should not affect the nulling performance of the interferometer [8]. Small defects should moreover be filtered out by the planned spatial filters.

4.4. Rhomb geometry and ghosts

The geometry of the rhomb (Fig. 8) is well constrained by the TIR optimal angle ($\theta' \approx 65^\circ$) and the dimension of the incoming interferometric beam, i.e. B$=$ 15 mm in diameter (the input face size E will be 20 by 20 mm). Each of the four rhombs must be strictly identical with arcsec precision for the angles and micrometric precision for the dimensions, which can be ensured to a certain degree by polishing them together in a same batch. Slight departure from nominal dimension will impact OPD, but can be compensated thanks to the thickness-adjustable beam splitters of the testbed which are also in *ZnSe*. In order to dump stray light originating from spurious reflections at the *ZnSe*/air interfaces, we chose to apply anti-reflective treatments ($R \approx 1.5\%$). Unfortunately, given the stringent constraints of nulling interferometry, we also had to apply well-chosen wedges between rhomb interfaces. In order to further mitigate ghosts, we have used ray-tracing analysis which led to an optimal wedge value of $w = 1^\circ$. Both rhombs of the double rhomb configuration possess the same but opposed wedge angle so that deviation and dispersion are annihilated and therefore do not impact the nulling process (Fig. 9). Let us also mention that the rhomb spacing D must be identical at the 0.1 mm-level between both interferometer arms in order to avoid differential dispersion of the OPD.

5. Manufacturing

In this section, we will present some manufacturing details for the *ZnSe* Fresnel rhomb APS.

5.1. ZnSe Rhomb cutting and polishing

We have conducted cutting and polishing trials of *ZnSe* rhombs with the appropriate global geometry and dimensions (Fig. 10). Results of ZYGO interferometric measurements in terms of surface quality comfortably fall in the specifications, and beyond our expectations with surface figures of $\lambda/100$ rms ($\lambda = 632.8$ nm). Concerning the roughness, WYKO profilometer measurements give a rather good 3 nm rms.

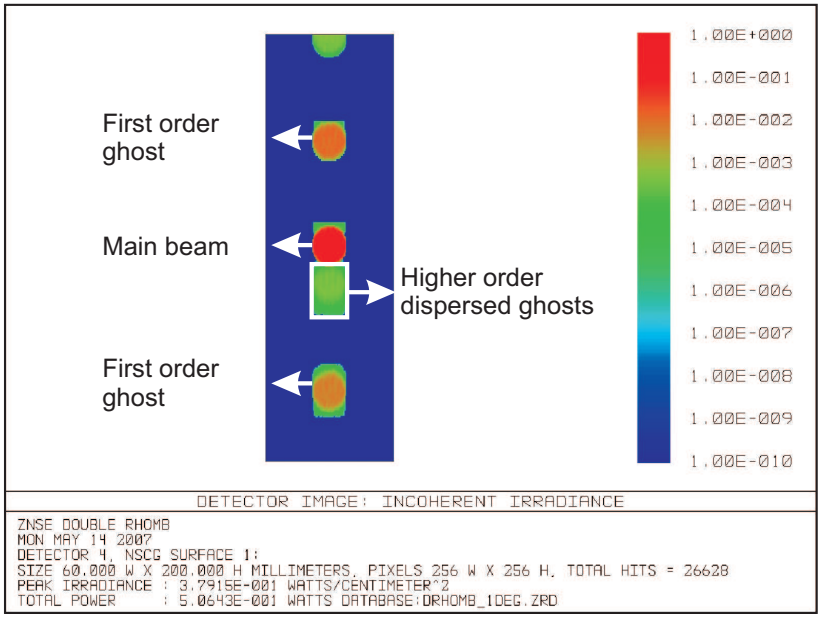

Fig. 9. ZEMAX ray-tracing analysis of a *ZnSe* double wedged (1°) rhomb.

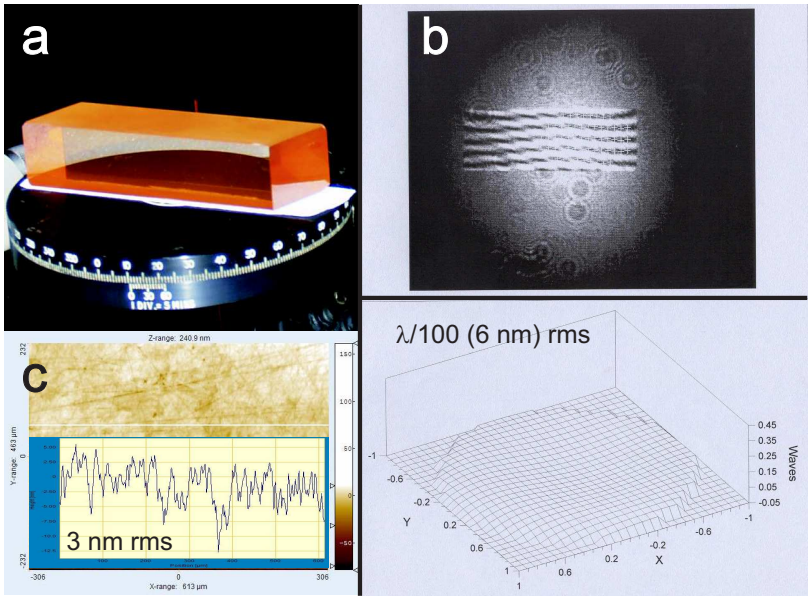

Fig. 10. a. Picture of a *ZnSe* Fresnel rhomb. b. ZYGO interferograms. c. WYKO profiles.

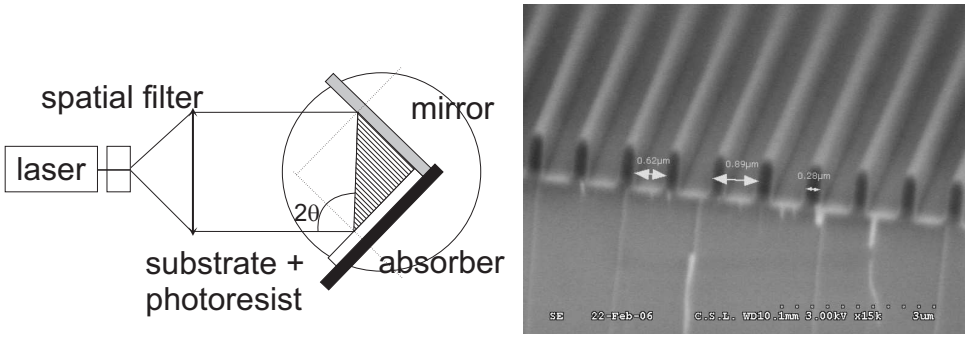

Fig. 11. Left: principle of holographic lithography (Lloyd mirror mounting). The grating period is inversely proportional to the angle between the two interferometer beams. Right: Micro-pattern on photoresist to be transferred by reactive plasma beam etching into the *ZnSe* substrate. The period and filling factor correspond to the design specifications.

5.2. TIR Grating manufacturing

We chose to manufacture the micro-pattern using holographic lithography and dry etching. The first one is necessary for masking the parts of the substrates to be protected during the etching step (Fig. 11, right). Direct laser writing or classical mask exposure techniques are not applicable onto the rhomb facets since they are designed to accommodate thin and flat substrates such as wafers for micro electronics. The holographic recording allows us to overcome this limitation by imprinting the photoresist mask thanks to a two-wave sinusoidal interference fringe pattern (Lloyd mirror mounting, Fig. 11, left). A good understanding and control of the recording and developing parameters (as energy dose, development duration, resist thickness, resist optical contrast, etc.) have produced reproducible rectangular binary profiles with a controlled filling factor (at the 10-nm level) instead of the natural sine profile. After its processing, the remaining photoresist pattern serves as a lithographic mask for the subsequent reactive plasma beam etching (RPBE) process, which makes use of both the ballistic effect and chemical reactivity of a beam of reactive ions to transfer structures into a substrate. The various parameters (gas melanges, beam energy, beam incidence, etc.) characterizing the etching process are optimized for the transfer into various materials. The interest of such a technique comes particularly from its high selectivity, the potential to efficiently etch one material and not another coexisting one, used as a mask. The infrared material (*ZnSe* or *CdTe*) is engraved using a selective chemistry (CH_4/H_2 [23] or chlorine-based [24] compounds), depending on the crystal phase of the material which leaves intact the photoresist mask but etches the infrared substrate. Validation trials are currently under progress. They aim at identifying the best process conditions ensuring the most efficient transfer of the diffractive structure from the mask into the material. Highest selectivity, homogeneity and reproducibility are the key factors under optimization.

5.3. Mechanical mount

The two mechanical mounts (one per interferometer arm) of the two *ZnSe* double rhombs must be thoroughly optimized to account for thermo-mechanical effects. Indeed, the component shall be measured at room (298 K) and cryogenic (100 K) temperatures. It will thus be cooled down and the mount must allow for an efficient heat transfer while compensating differential contractions. The alignment of the two rhombs must be controlled around 3 axes with an arcmin precision. The double rhomb spacing difference between both arms, and thus between the two corresponding mechanical mounts must be below 0.1 mm. The mounts must also account for

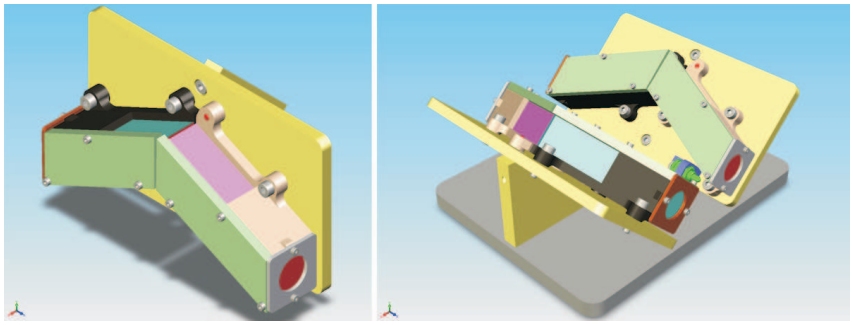

Fig. 12. Design of the *ZnSe* double Fresnel rhomb APS mechanical mounts. Right illustrates the practical implementation of the components in the interferometer at 45° from the test bench table, rotated of 90° from each other.

the *ZnSe* sensitivity to stress birefringence. In order to quantify the latter to help the mount design, a finite element analysis was conducted and resulted in the conclusion that the rhombs must lay freely at 45° in their mounts (Fig. 12). Indeed, given the stress-optics coefficient of *ZnSe*, $C_{\lambda=10.6\mu m} \approx -12$ brewsters [25], even its own weight constraint σ can induce a substantial birefringence $\Delta n = C_{\lambda=10.6\mu m}\sigma$ which is just within the specifications.

6. Measurement of a ZnSe Fresnel rhomb retardance at 632.8 nm

We conducted preliminary measurements of the performance of a *ZnSe* Fresnel rhomb at 632.8 nm with a simple polarimeter arrangement [26](Fig.13). A governing equation relates the ratio of the intensities $I^{\frac{\pi}{2}}$ (corresponding to P2$^{\frac{\pi}{2}}$) and I^0 (corresponding to P2^0) of the two orthogonal polarization states to the orientations of the input/output polarizer with respect to the retarder (α), and the retardance (Γ)

$$\frac{I^0}{I^{\frac{\pi}{2}}} = \frac{\sin^2 2\alpha \sin^2(\Gamma/2)}{1-\sin^2 2\alpha \sin^2(\Gamma/2)} \tag{3}$$

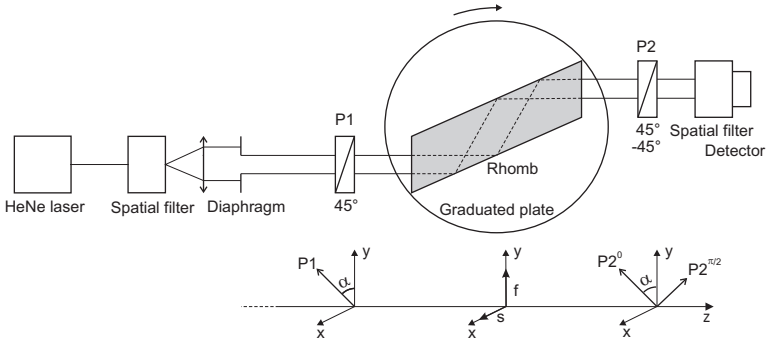

Fig. 13. Optical setup used to perform the *ZnSe* rhomb retardance measurement. Linearly polarized light (P1) is incident upon the rhomb, and the light emerges with an elliptical polarization. The intensities of the two orthogonal polarization states are measured by rotating the output polarizer (P2). s and f are respectively the slow and fast rhomb axis.

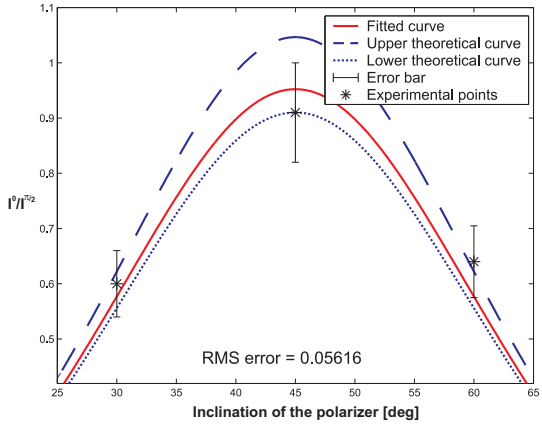

Fig. 14. *ZnSe* single rhomb retardance measurement. In blue: limits of the expected retardance vs polarizer inclinations. In red: fitted curve corresponding to a retardance of 88.8°±1.5°. The RMS error of the fit is 0.05616 and corresponds to a phase error of 1.5°, which is fully compliant with our setup precision.

In addition to the retardance measurement, the experiment allowed us to disentangle several parasitic effects that could prevent the rhomb to reach its theoretical phase shifting potential. The rhomb TIR angle of 65°±0.1° should theoretically provide a 91°±0.5° phase shift at 632.8 nm. The primary source of perturbation was identified as the surface and bulk scattering ($\sim 1\%$). Fortunately, we have demonstrated that it can be mitigated at least at the 10^{-5} level (accuracy of our optical setup) by inserting a spatial filter at the rhomb output, as planned for Nulltimate too. The secondary identified source was the spurious parasitic reflections. Tilting the rhomb by $\sim 1^{\circ}$ was necessary to get rid of the ghost, in agreement with our ray-tracing analysis that concluded to the necessity of wedging the final rhombs (Sect. 4.4). We have then measured a phase shift of 88.8°±1.5° [Fig.14] (uncertainty of the optical setup) which is consistent with the tilt-corrected theoretical value of 90.2°±0.5°(uncertainty of the measured rhomb angle). Given the different systematics in our experiment at 632.8 nm, we can extrapolate an upper boundary for the expectable null depth at 6 μm: $N < 10^{-4}$. Moreover, this experiment allowed us to identify the way to mitigate every potential sources of disturbance imputable to the sole rhomb APS so that its final performance should comply to the Darwin specifications.

7. Conclusion

To summarize, we have presented a new family of APS for thermal infrared radiations relying on the TIR phenomenon, modulated or not. The modulation can be induced either by an integrated subwavelength grating or a deposited thin film. Theoretical results show remarkable improvements over the classical Fresnel rhomb technique, which is always limited by the intrinsic dispersion of the bulk material used. We have also presented some design key points and encouraging preliminary measurements for the *ZnSe* prototype under manufacturing. In the framework of R&D activities for the Darwin mission, this prototype will be tested on the Nulltimate test bench at IAS. Results will be the subject of a forthcoming paper.

Acknowledgments

The authors acknowledge the financial support of ESA.